XRD, FTIR, AND THERMAL ANALYSIS OF BAUXITE ORE-PROCESSING WASTE (RED MUD) EXCHANGED WITH HEAVY METALS

Paola Castaldi[1],*, Margherita Silvetti[1], Laura Santona[1], Stefano Enzo[2], and Pietro Melis[1]

[1] Dipartimento di Scienze Ambientali Agrarie e Biotecnologie Agro-Alimentari, Sez. Chimica Agraria ed Ambientale, University of Sassari, Viale Italia 39, 07100 Sassari, Italy

[2] Dipartimento di Chimica, University of Sassari, Via Vienna 2, 07100 Sassari, Italy

Abstract—The present work shows the results of X-ray diffraction (XRD), Fourier transform infrared (FTIR), and thermal analysis of untreated (RM_{nt}) and acid-treated red mud (RM_a), a bauxite ore-processing waste, exchanged with Pb^{2+}, Cd^{2+}, and Zn^{2+} cations. These studies were performed in order to investigate the changes in the sorbent structure caused by the exchange with metals of different ionic radii.

The XRD pattern of RM_{nt}, analyzed according to the Rietveld method, showed a mixture of eight different phases. However, just three phases made up 78 wt.% of the RM_{nt}: cancrinite (33 wt.%), hematite (29 wt.%), and sodalite (16 wt.%). X-ray diffraction patterns of RM_{nt} exchanged with Pb^{2+} and Cd^{2+} cations revealed two additional phases, namely hydrocerussite [$Pb_3(CO_3)_2(OH)_2$ (10 wt.%)] and octavite [$CdCO_3$ (8 wt.%)].

These two phases probably originated from the carbonate precipitation processes which were due to the decarbonation of cancrinite. Hydrocerussite and octavite were not found in the case of acid-treated red mud samples.

In the FTIR spectra, the introduction of cations caused a distinct shift to higher wavenumbers in the peak at ~1100 cm^{-1}, which is attributed to the asymmetric stretch of Si$-$O$-$Al. This effect may be associated with the Pb^{2+}, Cd^{2+}, and Zn^{2+} adsorbed by the red muds which caused a deformation of the initial structure.

Thermal analysis data of the red mud samples were obtained by thermogravimetric/differential thermogravimetric analysis, and these methods were employed to evaluate the desorption behavior of water and to clarify the thermal stability of the chemical phases of the different red mud samples. The loss of metal-bound water in the red mud samples was found to depend on the size of non-framework cations and water loss consistently followed the order: $Zn^{2+}>Cd^{2+}>Pb^{2+}$.

Key Words—Cancrinite, Cations of Pb^{2+}, Cd^{2+}, and Zn^{2+}, Hydrocerussite, Octavite, Red muds, Sodalite.

INTRODUCTION

Red mud, a by-product of the alumina industry, is the alkaline material (pH 10.0−12.5) which remains after the digestion of bauxite with caustic soda during alumina extraction in the Bayer process (Phillips, 1998; Brunori *et al.*, 2005). Depending on the quality of bauxite, the quantity of red mud generated varies between 55 and 65% of the bauxite processed. Roughly 1.0−1.5 tons of red mud residue are produced for each ton of alumina and consequently millions of tons of caustic red mud are generated world-wide (Paramguru *et al.*, 2005). Red mud is a hazardous material, but, might also be considered a secondary raw material (*e.g.* because it contains rare earth elements), or as a potential geomedium for the fixation of contaminating materials, due to its alkaline pH and adsorptive capacity. Currently, red mud is usually dumped in holding ponds or dams (Lopez *et al.*, 1998). The possibility of using red mud as an adsorbent of heavy metals is of much interest because it could help to reduce the disposal of this residue and its

potential impact on the environment (Hind *et al.*, 1999; Sglavo *et al.*, 2000; Fuhrman, 2004). The combined presence in red mud of ferric, aluminum, and tectosilicate-like compounds is expected to be particularly effective in relation to the removal and immobilization of toxic heavy metals from waste waters and polluted soils (Apak *et al.*, 1998a; Gupta and Sharma, 2002; Komnitsas *et al.*, 2004; Santona *et al.*, 2006) or in the reduction of the leaching of soil nutrients (Summer *et al.*, 1996; Phillips, 1998).

The physical and chemical properties of red mud depend on the chemical and mineralogical composition of the bauxite (Komnitsas *et al.*, 2004) and on the conditions used in the alumina extraction. Consequently, the possibility of using red mud to reduce heavy-metal solubility can be established only after evaluation of its own chemical, physical, and structural properties. For such heterogeneous material, it is important to determine the main phases representing the active sites involved in the metal-fixation processes. It is also important to determine the mode of bonding of cations on the mineral surfaces of red mud and to identify the new chemical phases formed after the metal sorption. However, spectroscopic and thermal analyses of red muds exchanged with heavy metals are extremely limited

* E-mail address of corresponding author:
castaldi@uniss.it

461

because the phase constitution of this industrial waste is complex. In particular, recognizing and evaluating the structural changes occurring in red mud after exchange with heavy metals using XRD, FTIR, and thermal (TG/DTG) analyses represents a significant challenge.

Infrared spectroscopy can supply fundamental information on the changes in sorbent structure caused by the exchange with cations of different ionic radius, charge, and mass (Mozgawa *et al.*, 1999; Castaldi *et al.*, 2005). Thermal analysis can be employed to evaluate the desorption behavior of water in red mud exchanged with cations of different ionic radius (Joshi *et al.*, 2002). X-ray diffraction provides information about the nature of the constituent phases and structural changes occurring in the sorbent after exchange with heavy metals, and provides details on the structure and microstructure such as lattice parameters, average crystallite size, and microstrain.

The aim of this work was, therefore, to assess, through XRD, FTIR, and TG/DTG, the mineralogical and structural changes in untreated (RM_{nt}) and acid-treated (RM_a) red mud after exchange with cations of different chemical and physical properties.

MATERIALS AND METHODS

Characterization of the red mud

Red muds were obtained from the Ex-Eurallumina plant in Portovesme, SW Sardinia, Italy. The red muds were dried overnight at 105ºC, finely ground, and sieved to <0.02 mm (RM_{nt}). Red mud samples were also acid-treated (RM_a) by two washings with 0.05 M HCl for 2 h (ratio red mud/HCl solution 1:25 wt.%). After this treatment, RM_a samples were washed with distilled water and dried overnight at 105ºC. The acid treatment was performed to decrease the alkalinity of red mud and to obtain a sorbent that could be applied both in acidic and in neutral polluted soils.

The pH and electrical conductivity (EC) values were determined in a 1:25 ratio of sorbent/distilled water (Official Methods, 1999). The cation exchange capacity (CEC) was determined with $BaCl_2$-triethanolamine following national standard methods (Official Methods, 1999). The specific surface areas of the RM_{nt} and RM_a were determined by the BET/N_2 adsorption method (Carlo Erba Sorptomatic). The point of zero charge (PZC) of the RM_{nt} and RM_a samples was measured by Laser Doppler Velocimetry coupled with Photon Correlation Spectrometry using a Coulter Delsa 440 spectrometer equipped with a 5 mW He-Ne laser (632.8 nm) (Celi *et al.*, 2003). The total concentration of selected heavy metals in the RM_{nt} and RM_a samples was determined by drying the red mud overnight at 105ºC and digesting it with HNO_3 and HCl (ratio 1/3) in a Microwave Milestone MLS 1200. The heavy-metal concentrations were determined using a Beckam D.C. plasma atomic emission spectrometer.

Ion exchange

Adsorption studies were carried out in triplicate batches. All chemicals used were of reagent grade and used without additional purification. Samples of RM_{nt} and RM_a (1.0 g each) were treated separately with 25 mL of 0.2 M ionic solutions of Pb^{2+}, Cd^{2+}, and Zn^{2+}, all derived from their nitrate salts (Castaldi *et al.*, 2005). The sorbent/cationic solutions were shaken for 24 h at 200 rpm and 25ºC, which was proved beforehand to be sufficient for reaching equilibrium. Two other identical washings were carried out on the same red mud samples. The adsorption tests were carried out at controlled pH: a buffer solution of acetic acid-sodium acetate was used to maintain a constant pH (5.5) for Zn-, Pb-, and Cd-RM samples. After the ion-exchange process, the red mud samples were washed with 25 mL of distilled water.

After each step the solid and liquid phases were separated by centrifugation at 10,000 rpm for 20 min and the supernatant filtered through a 0.45 µm pore cellulose membrane filter. The samples obtained were air dried for 5−6 days. The total concentration of heavy metals sorbed by the RM samples was determined by drying the red mud overnight at 105ºC and digesting it with HNO_3 and HCl (ratio 1/3) in a Microwave Milestone MLS 1200. The heavy-metal concentrations were determined using a Beckam D.C. plasma atomic emission spectrometer. The data presented were the mean of three replicates.

Powder XRD analysis

X-ray powder diffraction (XRD) analysis was carried out using a Rigaku D/MAX diffractometer (CuKα). The operating power of the X-ray generator was 40 kV and 40 mA, the goniometer was equipped with a graphite diffracted-beam monochromator, and the patterns were collected in the angular range from 10º to 100º2θ with a step size of 0.05º2θ. Before analysis, polluted and non-polluted RM_{nt} and RM_a samples were dried at 65ºC for 8 h. After that, samples were dried at 140ºC for 8 h to eliminate humidity and weakly bound adsorbed water; then the XRD patterns of all the samples were recorded. The data collection was performed overnight (~12 h per pattern). For a scan of 90º2θ with step-size of 0.05º this is equivalent to ~24 s per point.

Crystalline phases were identified with a search-match procedure using the database of the International Center for Diffraction Data for Inorganic Substances (Inorganic Crystal Structure Database). The powder patterns were then analyzed quantitatively according to the Rietveld method (Young, 1993) using the *MAUD* software (Lutterotti and Gialanella, 1998) running on a personal computer. The estimated standard error of the phases is supplied by the procedure based on the assumption of a uniform and normal distribution of residuals, *i.e.* the difference between calculated and experimental intensity at each data point. Briefly, the

technique is sensitive to the presence of phases comprising 1–2 wt.% of the total, and the estimated standard error may be as large as 3–4 wt.% for the more abundant phases. This sensitivity is not to be ascribed to the numerical Rietveld method but mainly to the diffraction-pattern collection strategy.

Aside from crystalline phases, experience with the background behavior of XRD patterns suggests that ~15–20 wt.% of the RM consisted of amorphous oxides.

FTIR spectroscopy

The FTIR spectra in the 4000 to 400 cm^{-1} range were recorded at room temperature using a Nicolet 5 PC FTIR spectrometer equipped with *Omnic* software. Spectra were collected after 256 scans at 4 cm^{-1} resolution. The KBr pellet technique used for sample preparation utilized FTIR grade KBr (Fluka), dried at 200ºC for 24 h, 200 mg of which was ground together with 1 mg of RM sample (from the XRD analyses) for 1–2 min. The pellets were made by pressing 90 mg of the KBr-RM mixture in a die under vacuum for 4–6 min at 12 t pressure to produce transparent disks ~1 mm thick and 13 mm in diameter. An empty KBr pellet was used as reference and its spectrum was subtracted from the sample spectrum to suppress the spectral artifacts caused by KBr impurities and water.

Thermal analysis

Thermogravimetry (TG) and differential thermogravimetry (DTG) of the red mud samples were performed using a Netzsch STA 429 thermal analysis apparatus. The samples were heated in a platinum crucible in the temperature range 25–800ºC with a heating rate of 10ºC/min in air. The flow rate of air was 10 mL/min.

About 30 mg of the sample was used in each run. The water concentration in the samples was determined from the TG curve mass loss.

RESULTS AND DISCUSSION

Characterization of non-polluted RM_{nt} and RM_a samples

A mixture of eight phases was observed for the RM_{nt} sample, though it should be noted that just three phases made up 78 wt.% of the RM_{nt} sample, namely, cancrinite (ICSD #9317, S.G. $P6_3$, a = 1.275 nm, c = 0.514 nm), hematite (ICSD #15840, S.G. $R\bar{3}cH$, a = 0.5038 nm, c = 1.3772 nm), and sodalite (ICSD #29443, S.G. $P\bar{4}3n$, a = 0.882 nm) (Table 1).

Discriminating between cancrinite and sodalite, when present in the same sample, can be difficult because the phases have peak sequences which overlap. However, the two phases could be distinguished by the presence of at least three peaks, namely at d spacings of 0.463, 0.322, and 0.273 nm in cancrinite, which have no equivalent in sodalite (Figure 1). Cancrinite was the main phase of the red mud (33 and 29 wt.% for RM_{nt} and RM_a, respectively). With obvious caveats, because of the uncertainties in the quantitative determination, the percentage of cancrinite decreased and that of sodalite increased with acid treatment in the pattern of RM_a; the sodalite percentage was in fact greater in the RM_a sample (16 and 24 wt.% for RM_{nt} and RM_a, respectively) (Table 1). These two phases made up about half of the red mud. This is interesting because these two phases have never been reported together in previous studies, at least not in such large quantities (Paramguru *et al.*, 2005).

The cancrinite framework (hexagonal $P6_3$) consists of alternating Si-O-T units (T = Si or Al) deriving from SiO_4 and AlO_4 tetrahedra (Whittington *et al.*, 1998). The

Table 1. Main properties of red mud.

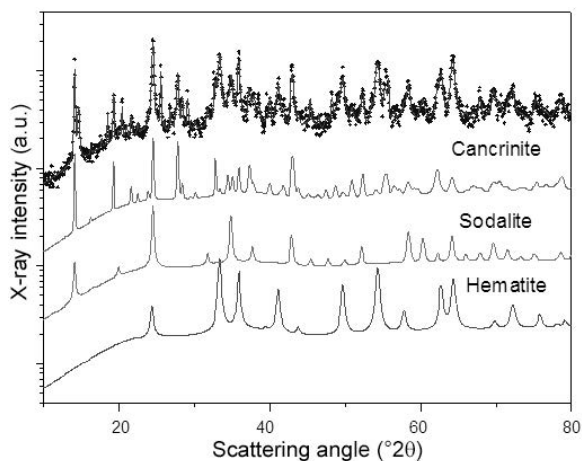| Chemical parameters	RM_{nt}	RM_a
pH	11.5	7.0
EC (mS/cm)	2.1	0.3
S_{BET} (m²/g)	18.9	25.2
CEC (mmol$_{(+)}$/kg)	106.5	98.2
PZC	5.1	5.3
Pb (mg/kg)	<0.01	<0.01
Cd (mg/kg)	<0.001	<0.001
Zn (mg/kg)	0.02	0.01
Cu (mg/kg)	23.9	21.4
V (mg/kg)	649.0	623.4
Cr (mg/kg)	790.0	786.5
Chemical phases		
Cancrinite [$Na_6Ca_{1.5}Al_6Si_6O_{24}(CO_3)_{1.6}$]	33.0	29.0
Sodalite [$Na_8(Cl,OH)_2Al_6Si_6O_{24}$]	16.0	24.0
Hematite [Fe_2O_3]	29.0	27.0
Boehmite [$AlO(OH)$]	6.0	5.0
Gibbsite [$Al(OH)_3$]	5.0	4.0
Anatase [TiO_2]	5.0	5.0
Andradite [Ca-Fe-Al-Si oxide]	4.0	4.0
Quartz [SiO_2]	2.0	2.0

Figure 1. Experimental XRD pattern (data points) and Rietveld refinement (solid line) of the RM_{nt} sample. The contributions of the three main phases are also reported after accomplishing the fit, according to their relative abundance.

tetrahedral arrangement determines the formation of cages and channels which are typical of the open porous structure of zeolites (Hackbarth *et al.*, 1999; Castaldi *et al.*, 2005). The wide main channel can host cations and anions such as carbonate, whereas the small cages contain only cations and water molecules (Mon *et al.*, 2005). Sodalite differs from cancrinite in terms of the presence of OH^- and Cl^- compensating anions in place of the carbonate, in terms of its symmetry of crystallization (cubic $P\bar{4}3n$), and because of the absence of channels in its framework which are replaced by a network of large cages which can accommodate cations or water molecules (Barrer *et al.*, 1970; Zheng *et al.*, 1997; Mon *et al.*, 2005).

Hematite was not unexpected due to the red color of the red mud and it represented 29 and 27 wt.% of the RM_{nt} and RM_a samples, respectively (Table 1).

Quantities of boehmite and gibbsite (11 wt.% and 9 wt.% of the RM_{nt} and RM_a samples, respectively) were also detected. These phases were not unexpected either because they are probably derived from the processing of bauxite and represent a fraction of aluminum hydroxides which were not completely extracted. Clearly the quartz and andradite phases were connected to the mineralogical features of the extraction site. Moreover, note the weak but appreciable presence of titanium in the form of anatase (Table 1). A specific investigation on this phase may be interesting because of its well known photocatalytic property.

A significant variation in the lattice parameters of the cancrinite after the acid treatment was observed (Table 2), where the *c* axis varied from 0.514 nm in the RM_{nt} to 0.516 nm in the RM_a sample. This increase may be due to the partial dissolution of intracrystalline carbonate anions which are placed in the main channel of cancrinite along the direction of the hexagonal *c* axis (Hackbarth *et al.*, 1999). This was also reflected by the increase in the specific surface area of RM_a (Table 1) due to the 'cleaning effect' of HCl treatment, which partially dissolved the cancrinite (Santona *et al.*, 2006).

The PZC values of the RM_{nt} and RM_a samples were 5.1 and 5.3, respectively, which is significantly different from the values found in the literature (PZC = 8−8.5)

(Apak *et al.*, 1998b; Lopez *et al.*, 1998; Pradhan *et al.*, 1999); this is probably due to the large aluminosilicate content of this material.

XRD analysis of RM_{nt} samples exchanged with Zn^{2+}, Pb^{2+}, and Cd^{2+} cations

The maximum amount of heavy metals adsorbed on RM_{nt} followed the order: Zn^{2+} > Pb^{2+} > Cd^{2+} (Santona *et al.*, 2006). In general, adsorbing phenomena were likely to involve the three main phases, *i.e.* hematite, cancrinite, and sodalite. Given the known stability of hematite, the latter two phases may be responsible for the observed reactivity with the added cations. Cancrinite and sodalite are tectosilicates that had a negative charge density in their lattice because of substitution of Si^{4+} by Al^{3+} (Whittington *et al.*, 1998; Mon *et al.*, 2005). This negative charge density could have been neutralized by metals adsorbed with outer-sphere bonds on the external surfaces and by the incorporation of metals in the cages and channels of these aluminosilicate frameworks.

The mineralogical and structural changes occurred on the RM_{nt} after the exchange, immobilization, and precipitation reactions with the heavy metals were determined through the XRD analysis.

The RM_{nt} exchanged with Zn nitrate showed that the mineralogical composition did not change substantially with respect to the untreated red mud (figure not shown, Table 3). In addition, smithsonite or other carbonate forms of zinc were not observed, probably because carbonate forms of Zn are not stable at the working pH conditions.

Comparison of the lattice parameters of sodalite and cancrinite for the untreated and treated red mud and for the red muds exchanged with heavy metals (Table 2) revealed that the lattice parameter of cubic sodalite in Zn-RM_{nt} was significantly smaller than that found in the untreated red mud. This may be due to an incorporation of Zn^{2+} into the structural cages of sodalite, which caused a contraction of lattice parameters due to the significantly smaller ionic radius of Zn^{2+} (0.74 Å) which exchanged for Na^+ cations (1.02 Å).

Table 2. Lattice parameters of the main constituents of RM_{nt} and RM_a (error associated with the unit-cell parameters ±0.001).

	Cancrinite (SG $P6_3$)		Sodalite (SG $P\bar{4}3n$)	Hematite (SG $R\bar{3}c$)	
	a (nm)	*c* (nm)	*a* (nm)	*a* (nm)	*c* (nm)
RM_{nt}	1.266	0.514	0.896	0.503	1.375
RM_a	1.266	0.516	0.896	0.502	1.375
Zn-RM_{nt}	1.266	0.516	0.887	0.503	1.374
Cd-RM_{nt}	1.265	0.516	0.892	0.503	1.375
Pb-RM_{nt}	1.270	0.517	0.907	0.503	1.375
Zn-RM_a	1.264	0.516	0.890	0.503	1.374
Cd-RM_a	1.266	0.517	0.893	0.503	1.376
Pb-RM_a	1.270	0.517	0.904	0.503	1.375

Table 3. Mineralogical phases of RM_{nt} and RM_a exchanged with Zn^{2+}, Cd^{2+}, and Pb^{2+} (wt.%) (140ºC).

	$Zn-RM_{nt}$	$Cd-RM_{nt}$	$Pb-RM_{nt}$	$Zn-RM_a$	$Cd-RM_a$	$Pb-RM_a$
Cancrinite	30.0	20.0	20.0	28.0	27.0	27.0
Sodalite	19.0	23.0	23.0	23.0	23.0	24.0
Hematite	29.0	27.0	25.0	27.0	28.0	27.0
Bohemite	6.0	6.0	6.0	6.0	6.0	6.0
Gibbsite	5.0	5.0	5.0	5.0	5.0	5.0
Anatase	5.0	5.0	5.0	5.0	5.0	5.0
Andradite	4.0	4.0	4.0	4.0	4.0	4.0
Quartz	2.0	2.0	2.0	2.0	2.0	2.0
Octavite	–	8.0	–	–	–	–
Hydrocerussite	–	–	10.0	–	–	–

After the addition of Cd nitrate to the RM_{nt}, octavite [$CdCO_3$ (8 wt.%)] was observed in the XRD pattern (Figure 2). Its contribution to the total Rietveld fit was evaluated numerically and is presented in Figure 2. Furthermore, in the RM_{nt} exchanged with Cd, a decrease of cancrinite and an increase in sodalite were observed with respect to the untreated red mud (Table 3). It is possible that the process of decarbonation of cancrinite generated octavite, also favoring the formation of sodalite.

Similar conclusions may be drawn for the pattern of RM_{nt} treated with Pb nitrate, where a 10 wt.% presence of hydrocerussite [$Pb_3(CO_3)_2(OH)_2$] was observed

(Table 3). Note that a complete structure solution of hydrocerussite was reported only recently (Martinetto et al., 2002). Figure 2 shows the contribution of hydrocerussite numerically isolated from the rather complex experimental pattern after the Rietveld fitting.

Furthermore, the $Pb-RM_{nt}$ sodalite phase showed an expanded lattice volume, which can be considered significant with respect to the RM_{nt} ($a0$ +0.011 nm for Pb^{2+}). The unit-cell expansion may be associated with the incorporation of Pb^{2+} ions, which have an ionic radius substantially greater (1.19 Å) than the Na^+ ions (1.02 Å) for which they were exchanged. Nevertheless,
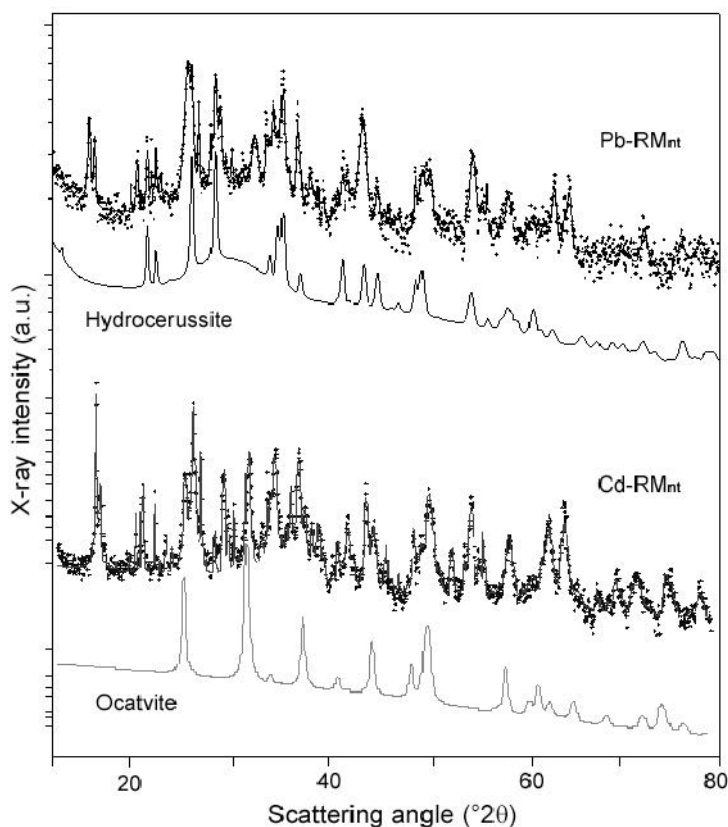
Figure 2. Data points of experimental XRD patterns and full lines after Rietveld refinement for the $Cd-RM_{nt}$ and $Pb-RM_{nt}$ samples.
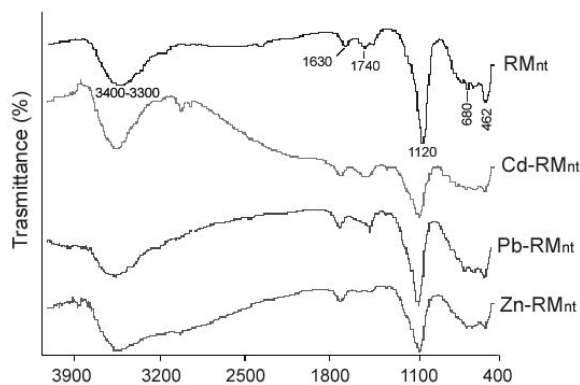
Figure 3. FTIR spectra of undoped and doped RM_{nt} samples.

Figure 4. FTIR spectra of undoped and doped RM_a samples.

the small changes in the lattice parameters derived when Pb^{2+} exchanges for Na^+ could be due to the difficulty experienced by divalent cations in accessing exchangeable sites. Besides, no evidence for such behavior was observed in specimens treated with Cd^{2+}, though some cationic incorporation cannot be excluded.

XRD analysis of RM_a samples exchanged with Zn^{2+}, Pb^{2+}, and Cd^{2+} cations

The maximum metal adsorption on RM_a followed the order: $Zn^{2+} > Cd^{2+} > Pb^{2+}$ (Santona *et al.*, 2006). The addition of Zn^{2+} affected the lattice-contraction parameters in sodalite while the opposite behavior was observed in $Pb-RM_a$ (Table 2). In the case of $Cd-RM_a$ no appreciable changes were observed. Note that acid pretreatment precluded the formation of octavite and hydrocerussite (Table 3). These phases were absent from the XRD patterns of RM_a exchanged with Cd^{2+} and Pb^{2+} (figures not shown).

FTIR spectra analysis

Shifts in frequencies and variations in the intensity of some bands were observed in RM_{nt} and RM_a samples exchanged with different metals. These changes depended on cation exchange, but clear correlations were lacking (Figures 3−4).

In all the spectra a strong band was present in the hydroxyl-stretching region at $3400-3300$ cm^{-1}. This was probably due to the presence of H_2O in the red mud (Armstrong and Dann, 2000; Ruan *et al.*, 2001; Gök *et al.*, 2007). In all the samples a band at ~1630 cm^{-1} was detected. This was attributed to the water molecules occluded inside the aluminosilicate structure (Linares *et al.*, 2005; Gök *et al.*, 2007).

Carbonate bands were observed within the 1410−1470 cm^{-1} region. In particular, in the traces for $Pb-RM_{nt}$ and $Cd-RM_{nt}$, the peak at ~1440 cm^{-1} was more intense. This is in agreement with the XRD data where two carbonate phases (octavite and hydrocerussite) were observed for these samples. The peak recorded at 1400 cm^{-1} in the RM_{nt} and RM_a samples could be
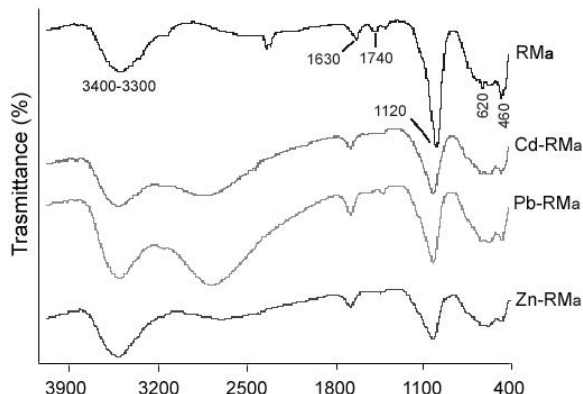
attributed to nitrate; this NO_3^- band might be present in both cancrinite and sodalite, according to the results reported by Zhao *et al.* (2004).

Even though several studies have distinguished sodalite and cancrinite, using FTIR spectroscopy (*e.g.* Barnes *et al.*, 1999; Armstrong and Dann, 2000), this seems very difficult with a material as heterogeneous as the red mud. Sodalite and cancrinite, being very similar in terms of their structural features, show common peaks in the region $400-500$ cm^{-1} due to the $T-O$ bend (where T = Si or Al) and in the region $560-630$ cm^{-1} due to 4- or 6-membered ring vibrations of SiO_4 or AlO_4 tetrahedra (Barnes *et al.*, 1999) (Figures 3−4). Moreover, in all the RM spectra, a peak due to stretching vibrations of the $Fe-O$ bond ($460-500$ cm^{-1} range) was also present (Ruan *et al.*, 2001). Additional peaks were also observed in the region $680-600$ cm^{-1} (Figures 3−4) due to the symmetric stretch of the $Si-O-Al$ framework and at $1100-1120$ cm^{-1} due to the asymmetric stretch of the $Si-O-Al$ framework (Barnes *et al.*, 1999). The FTIR spectra of the RM_{nt} and RM_a heavy metal-doped samples showed slight differences with respect to the untreated sample; in particular the peak at ~1100 cm^{-1} shifts slightly to greater wavenumbers (Figures 3−4). This effect, which is indicative of a decreased strength of the $Si-O-Al$ bond (Mozgawa *et al.*, 2002), may be associated with the cation-exchange process which implies the initial structure to be deformed. Finally, in the RM_a-doped samples, the peak at 1470 cm^{-1} appears lowered in its intensity as a result of both the acid pre-treatment and the metal-nitrate salts used as doping solutions which favored the dissolution of carbonates. These results are consistent with those obtained from the XRD analysis of RM_a.

Thermal behavior

Weight losses for the RM_{nt} and RM_a samples were detected at similar stages. The weight loss measured in the temperature range 60−150ºC was attributed to the superficial absorbed water, with the temperature of the peak

Table 4. Weight losses (percentage of total sample weight) recorded by the TG analysis.

	60−150ºC	240−310ºC	310−490ºC	490−800ºC
RM_{nt}	1.89	2.18	1.03	1.44
RM_a	1.87	2.19	1.11	1.39
$Zn-RM_{nt}$	2.10	2.92	1.03	1.22
$Cd-RM_{nt}$	1.75	2.32	1.35	1.36
$Pb-RM_{nt}$	1.68	2.20	1.57	1.18
$Zn-RM_a$	2.27	2.73	1.11	1.25
$Cd-RM_a$	2.07	2.29	1.10	1.27
$Pb-RM_a$	2.08	2.20	1.12	1.29

varying (Figure 5). The RM_{nt} and RM_a exchanged with Zn^{2+} in particular had greater weight losses (Table 4).

The weight losses in the 240−490ºC range can be interpreted mainly as the sum of a number of events. The first (240−310ºC range) with a peak at 273ºC may be associated with the loss of water molecules located in the channels and cages of the cancrinite and sodalite structure and bound to the non-framework cations (Castaldi *et al.*, 2005). In Figures 5 and 6, the peak at 273ºC varies in intensity depending on the metal being considered. The weight losses in the RM_{nt} and RM_a doped samples in the range 240−310ºC decreased with increase in the size of non-framework cations exchanged and they consistently followed the order $Zn^{2+}>Cd^{2+}>Pb^{2+}$. The ionic radii of these metals increase in the same order. This was expected because the possibility that each metal must interact with the sorbent reactive sites depends on its charge density, which is a consequence of the ion size. Thus the greater weight losses recorded in both $Zn-RM_{nt}$ and $Zn-RM_a$ samples are due to the greater sphere of hydration of Zn^{2+} ions which are the smallest of the three metals tested.

The thermal events recorded in the range 310−490ºC can be ascribed to a synergic release of CO_3^{2-} groups (Linares *et al.*, 2005) and to the decomposition of gibbsite (Pontikes *et al.*, 2007). In the $Pb-RM_{nt}$ and $Cd-RM_{nt}$ samples, the peak at 330−350ºC seems to increase due to the partial release of carbonate groups by the precipitated Pb^{2+} and Cd^{2+} carbonate compounds hydrocerussite and octavite. In all RM_a samples this peak is markedly decreased in its intensity, probably because the acid pre-treatment favored the dissolution of carbonates and gibbsite, in agreement with the XRD results and FTIR analysis of RM_a.

The peak at ~500ºC observed in all the RM samples can be assigned to the dehydration of boehmite to form aluminum oxide phases (Sglavo *et al.*, 2000).

In the $Cd-RM_{nt}$ sample another peak is present at ~600ºC which may be attributed to the total decomposition of octavite. By contrast, the degradation of the Pb-carbonate was not identified by precise peaks but by a progressive weight loss which took place in the 310−490ºC temperature range.

CONCLUSIONS

The adsorbing properties of red mud are related to its capacity to decrease the mobility of heavy metals through exchange and precipitation reactions. These aspects are of particular importance in evaluating the efficiency of the red mud as a heavy-metal adsorbent.
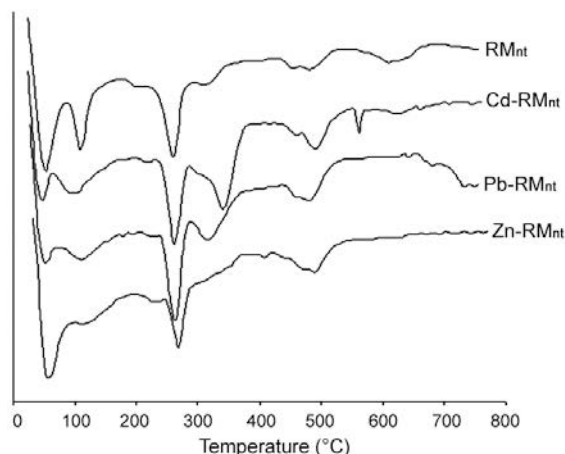

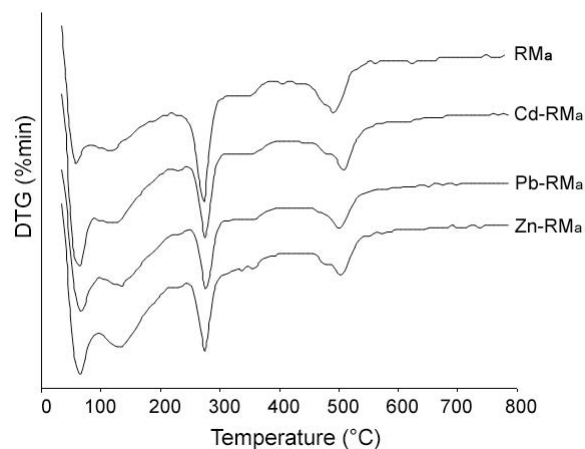Figure 5. DTG thermograms of undoped and doped RM_{nt} samples.

Figure 6. DTG thermograms of undoped and doped RM_a samples.

The XRD analysis, coupled with the Rietveld method, was found to be particularly suitable for identifying and quantifying the new carbonatic phases (octavite and hydrocerussite) in the red mud doped with Cd and Pb nitrates. This result is particularly significant and seems more important in terms of the fixation of heavy metals than in terms of structural entrapment. Besides, the carbonate precipitation process was not observed in the case of acid-treated red muds probably because of the partial dissolution of intracrystalline carbonate anions which reside within the main channel of cancrinite.

The essential changes observed in the FTIR spectra of red mud samples exchanged with Pb^{2+}, Cd^{2+}, and Zn^{2+} cations may be related to the greater degree of cancrinite and sodalite-ring deformation, which is caused by the incorporation of cations with larger ionic radii. In particular, the 12-membered rings in cancrinite appear to be the most favorable for incorporation of hydrated cations. However, the insertion of these groups in a specific site as opposed to ε-cages or β-cages of sodalite is difficult to determine from our XRD data-fitting analysis.

The thermoanalytical data obtained from TG/DTG showed that in the doped RM samples the water loss decreased with increase in the size of exchanging non-framework cations. This was explained by the regularity of the network formed by water molecules and the extent of various water molecule interactions.

REFERENCES

Apak, R., Tutem, E., Hugul, M., and Hizal, J. (1998a) Heavy metal cation retention by unconventional sorbents (red mud and fly ashes). *Water Research*, **32** , 430−440.

Apak, R., Güçlü, K., and Turgut, M.H. (1998b) Modeling of copper(II), cadmium(II) and lead(II) adsorption on red mud. *Journal of Colloid and Interface Science*, **203**, 122−130.

Armstrong, J.A. and Dann, S.E. (2000) Investigation of zeolite scales formed in the Bayer process. *Microporous and Mesoporous Materials*, **41**, 89−97.

Barnes, M.C., Addai-Mensah, J., and Gerson, A.R. (1999) A methodology for quantifying sodalite and cancrinite phase mixtures and kinetics of the sodalite to cancrinite phase transformation. *Microporous and Mesoporous Materials*, **31**, 303−319.

Barrer, R.M., Cole, J.F., and Villiger, H. (1970) Chemistry of soil minerals. Part VII. Synthesis, properties, and crystal structures of salt-filled cancrinite. *Journal of the Chemical Society*, **A3**, 1523−1531.

Brunori, C., Cremisini, C., Massanisso, P., Pinto, V., and Torricelli, L. (2005) Reuse of treated red mud bauxite waste: studies on environmental compatibility. *Journal of Hazardous Materials*, **117**, 55−63.

Castaldi, P., Santona, L., Cozza, C., Giuliano, V., Abruzzese, C., Nastro, V., and Melis, P. (2005) Thermal and spectroscopic studies of zeolites exchanged with metal cations. *Journal of Molecular Structure*, **734**, 99−105.

Celi, L., De Luca, G., and Barberis, E. (2003) Effects of interaction of organic and inorganic P with ferrihydrite and kaolinite-iron oxide systems on iron release. *Soil Science*, **168**, 479−488.

Fuhrman, H.G. (2004) Arsenic removal from water using seawater-neutralised red mud (Bauxsol). PhD thesis, Environment & Resources DTU Technical University of Denmark.

Gök, A., Omastová, M., and Proke J. (2007) Synthesis and characterization of red mud/polyaniline composites: Electrical properties and thermal stability. *European Polymer Journal*, **43**, 2471−2480.

Gupta, V.K. and Sharma, S. (2002) Removal of cadmium and zinc from aqueous solutions using red mud. *Environmental Science and Technology*, **36**, 3612−3617.

Hackbarth, K., Gesing, T.M., Fechtelkord, M., Stief, F., and Buhl, J.-Ch. (1999) Synthesis and crystal structure of carbonate cancrinite $Na_8[AlSiO_4]_6CO_3(H_2O)_{3.4}$, grown under low-temperature hydrothermal conditions. *Microporous and Mesoporous Materials*, **30**, 347−358.

Hind, A.R., Bhargava, S.K., and Grocott, S.C. (1999) The surface chemistry of Bayer process solids: a review. *Colloids and Surfaces A, Physicochemical and Engineering Aspects*, **146**, 359−374.

Joshi, U.D., Joshi, P.N., Tamhankar, S.S., Joshi, V.P., Idage, B.B., Joshi, V.V., and Shiraljar, V.P. (2002) Influence of the size of extraframework monovalent cations in X-type zeolite on their thermal behavior. *Thermochimica Acta*, **387**, 121−130.

Komnitsas, K., Bartzas, G., and Paspaliaris, I. (2004) Efficiency of limestone and red mud barriers: laboratory column studies. *Minerals Engineering*, **17**, 183−194.

Linares, C.F., Sánchez, S., Urbina de Navarro, C., Rodríguez, K., and Goldwasser, M.R. (2005) Study of cancrinite-type zeolites as possible antiacid agents. *Microporous and Mesoporous Materials*, **77**, 215−221.

Lopez, E., Soto, B., Arias, M., Nunez, A., Rubinos, D., and Barral, M.T. (1998) Adsorbent properties of red mud and its use for wastewater treatment. *Water Research*,**, 32**, 1314−1322.

Lutterotti, L. and Gialanella, S. (1998) X-ray diffraction characterization of heavily deformed metallic specimens. *Acta Materialia*, **46**, 101−110.

Martinetto, P., Anne, M., Dooryhée, E., Walter, P., and Tsoucaris, G. (2002) Synthetic hydrocerussite, $2PbCO_3 \cdot Pb(OH)_2$, by X-ray power diffraction. *Acta Crystallographica Section A*, **C58**, i82−i84.

Mon, J., Deng, Y., Flury, M., and Harsh, J.B. (2005) Cesium incorporation and diffusion in cancrinite, sodalite, zeolite and allophone. *Microporous and Mesoporous Materials*, **86**, 277−286.

Mozgawa, W., Sitarz, M., and Rokita, M. (1999) Spectroscopic studies of different aluminosilicate structures. *Journal of Molecular Structure*, **511,** 251−257.

Mozgawa, W., Fojud, Z., Handke, M., and Jurga, S. (2002) MAS NMR and FTIR spectra of framework aluminosilicates. *Journal of Molecular Structure*, **614**, 281−287.

Official Methods, No III. 1 Ordinary Suppl. Italian G.U. No. 248 of 21/10/1999.

Paramguru, R.K., Rath, P.C., and Misra, V.N. (2005) Trends in red mud utilization − a review. *Mineral Processing and Extractive Metallurgy Review*, **26**, 1−29.

Phillips, I.R. (1998) Use of soil amendments to reduce nitrogen, phosphorus and heavy metal availability. *Journal of Soil Contamination*, **7**, 191−212.

Pontikes, Y., Nikolopoulos, P., and Angelopoulos, G.N. (2007) Thermal behaviour of clay mixtures with bauxite residue for the production of heavy-clay ceramics. *Journal of the European Ceramic Society*, **27**, 1645−1649

Pradhan, J., Das, S.N., and Thakur, R.S. (1999) Adsorption of hexavalent chromium from aqueous solution by using activated red mud. *Journal of Colloid and Interface Science*, **217**, 137−141.

Ruan, H.D., Frost, R.L., and Kloprogge, J.T. (2001) The behavior of hydroxyl units of synthetic goethite and its

dehydroxylated product hematite. *Spectrochimica Acta, Part A*, **57**, 2575−2586.

Santona, L., Castaldi, P., and Melis, P. (2006) Evaluation of the interaction mechanisms between red muds and heavy metals. *Journal of Hazardous Materials*, **136**, 324−329.

Sglavo, V.M., Campostrini, R., Maurina, S., Carturan, G., Monagheddu, M., Budroni,G. and Cocco, G. (2000) Bauxite red mud in the ceramic industry. Part 1: thermal behaviour. *Journal of the European Ceramic Society*, **20**, 235−244.

Summer, R.N., Smirk, D.D., and Karafilis, D. (1996) Phosphorus retention and leachates from sandy soil amended with bauxite residue (red mud). *Australian Journal of Soil Research*, **34**, 555−567.

Whittington, B.I., Fletcher, B.L., and Talbot, C. (1998) The effect of reaction conditions on the composition of desilication product (DSP) formed under simulated Bayer conditions. *Hydrometallurgy*, **49**, 1−22.

Young, R.A. (1993) *The Rietveld Method*. Oxford University Press, Oxford, UK.

Zhao, H.T., Deng, Y.J., Harsh. J.B., Flury, M., and Boyle, J.S. (2004) Alteration of kaolinite to cancrinite and sodalite by simulated Hanford tank waste and its impact on cesium retention. *Clays and Clay Minerals*, **52**, 1−13.

Zheng, K., Gerson, A.R., Addai-Mensha, J., and Smart, R. (1997) The influence of sodium aluminosilicate crystallisation and solubility in sodium aluminate solutions. *Journal of Crystal Growth*, **171**, 197−208.